



Water vapour permeation through high barrier materials: numerical simulation and comparison with experiments

A. Batard^{1,2} , E. Planes² , T. Duforestel¹ , L. Flandin^{2,*} , and B. Yrieix³ 

¹ EDF R&D, ENERBAT, EDF Lab Les Renardières, 77818 Moret-Loing-et-Orvanne, France

² LEPMI, LMOPS, Université de Savoie, Campus Savoie Technolac, Hélios, 73376 Le Bourget-du-Lac, France

³ EDF R&D, MMC, EDF Lab Les Renardières, 77818 Moret-Loing-et-Orvanne, France

Received: 10 November 2017

Accepted: 13 March 2018

Published online:
20 March 2018

© Springer Science+Business Media, LLC, part of Springer Nature 2018

ABSTRACT

The long-term thermal performance of vacuum insulation panels (VIP) is brought by the capacity of their barrier envelope to maintain the core material under vacuum. This study is focused on the detailed modelling of gas transfer through the defects of aluminium-coated polymer films used for VIPs' envelopes. The 3D simulations were performed with monolayer and multilayer metal-coated polymer films. They have been carried out in dynamic conditions with the SYRTHES® software developed by EDF R&D. The results show that the water vapour and air permeations through a monolayer film slightly depend on the polymer substrate thickness, diffusivity and solubility, but primarily, on the defects geometry and arrangement. Regarding multilayer films, the permeation can be deduced from the ideal laminate theory. We are now able to provide and operate a numerical model, which can calculate the permeance of monolayer or multilayer metallized polymer films as a function of the coating quality and the geometry of the layers. Even if calculated permeances are ten times higher than measurements, this study improves our understanding of gas transports through VIPs' barrier envelope and allows to manage more efficiently the relations between the films microstructures and their overall permeability. This paper is split into 6 parts: physical phenomena, methodology and modelling tools, simulation results, experiments and model validation and then, discussion and conclusion.

Address correspondence to E-mail: lionel.flandin@univ-savoie.fr

List of symbols

Greek letters

- λ Thermal conductivity ($\text{W m}^{-1} \text{K}^{-1}$)
 ϕ_i Mass flux density of gas i (kg s^{-1})
 Π_i Permeance to the gas i ($\text{kg m}^{-2} \text{s}^{-1} \text{Pa}^{-1}$)
 ρ Density (kg m^{-3})

Other symbols

- \emptyset Defect diameter (m)

Physical constants

- k_B Boltzmann's constant ($1.381 \times 10^{-23} \text{J K}^{-1}$)
 r_i Specific gas constant of gas i ($\text{J kg}^{-1} \text{K}^{-1}$)

Roman letters

- c_i Concentration of a gas i (kg m^{-3})
 c_p Specific heat capacity ($\text{J kg}^{-1} \text{K}^{-1}$)
 D_K Knudsen coefficient ($\text{m}^2 \text{s}^{-1}$)
 $D_{i,j}$ Diffusion coefficient of gas i in material j ($\text{m}^2 \text{s}^{-1}$)
 e_{poly} Polymer thickness (m)
 FSD Surface fraction of defects (%)
 k Scale factor (–)
 L Distance between defects (m)
 l Barrier complex's thickness (m)
 m_i Molecular mass of gas i (kg)
 p_i Partial pressure of gas i (Pa)
 $S_{i,j}$ Solubility coefficient of gas i in material j ($\text{kg m}^{-3} \text{Pa}^{-1}$)
 T Temperature (K)

Introduction

When they are used for building thermal insulation, VIPs require long service life. Requirements for other applications like cold shipping boxes, refrigerators or freezers are in comparison very limited. Temperature-controlled transportation and pharmaceutical, aerospace and automotive industries expect a service life ranging from month to years. For typical building insulation it should be significantly larger and reach up to 50 years [1–3]. This performance relies both on the nanoporous property of the core material and on the barrier envelope that prevents the increase in moisture and internal pressure. The use of VIPs for building thermal insulation requires films with extreme barrier properties [1, 4, 5].

The current study especially concerns the 3D modelling of the gas diffusion through VIPs' envelope. Two types of envelopes can be used: laminated aluminium foils, or high barrier metalized polymer membranes. Only the second type is considered here. In practice, the appropriate level of barrier performance can only be reached by stacking two to three coated polymer films [6]. A sealing layer of PE or PP is generally added to this complex (cf. Fig. 1).

The barrier performance of VIPs' envelopes basically relies on the thickness of the coating layers [7]. Nevertheless the high thermal conductivity of the metal layer makes aluminium foil or thick aluminium layer nonacceptable for the application. A good compromise has actually to be found between barrier performance and thermal bridges. Coated polymeric films are a good solution because very thin metallic layer can be deposited with great care. The physical vapour deposition (PVD) process generally induces very homogeneous and well-controlled layers. However, a close analysis with a high-resolution microscope always reveals the presence of pinholes [7]. Although very small (in the submicron scale) and representing a very small fraction of the film surface (far below 1%), these defects are held responsible for the flux of molecules through within the VIP. The aim of this paper is to explain the relationship between the coating layer defect characteristics and its permeation performance.

Monolayer film configurations are studied first. It is composed of three materials: the polymer substrate, the aluminium coating and the material which might fill the defects. In a second step, multilayer film configurations are studied to evaluate the impact of stacking. The current study is focused on the water vapour permeation, but the same evaluations could be carried out for any other gas permeation. For water vapour diffusion, a partial pressure difference of 2000 Pa is imposed. This value is usually used for

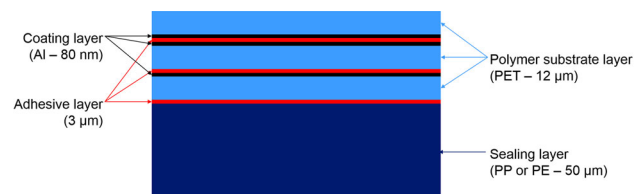


Figure 1 Typical composition of a barrier complex for VIP's envelope.

experimental permeance measurements at ambient temperature.

As presented in the literature [8–11], simulations were performed to understand the relationships between defect characteristics and gas permeation through the entire coated layer. The significant characteristics of the defects should first be determined experimentally. The polymer permeance also needs to be considered.

The paper is split into 6 parts. In the first two parts physical phenomena, modelling methodology and modelling tools are described. The third part is devoted to the presentation of simulation results. In the fourth part, the experimental results are introduced and the models relevancy is discussed. And then, the two final parts are devoted to the discussion and the conclusion about the results and the modelling approach.

Gas dissolution and diffusion phenomena in metallized polymer membranes

Gas dissolution and diffusion into the polymers

The gaseous flux results from a gas pressure difference imposed between the sides of the polymer. This flow is the result of three phenomena: gas dissolution on one side of the membrane, gas diffusion through the polymer layer and desorption on the other side. The sorption phenomenon (adsorption and desorption) is described by Henry's law [12–14]. At the equilibrium, the concentration c_i of a gas i in a polymer j is linked to the gas partial pressure p_i on its surface by the solubility coefficient $S_{i,j}$.

$$c_i = S_{i,j} p_i \quad (1)$$

In polymers, the gas flow can be represented with the Fick's law [12, 13, 15]. The gas flow depends on the concentration gradient and the diffusion coefficient $D_{i,j}$.

$$\vec{\varphi}_i = -D_{i,j} \vec{\nabla} c_i \quad (2)$$

In the case of a two-layer polymer assembly, it is possible to observe that the concentration gradient of the gas is not continuous when the nature of the polymer changes at the interface, because their solubility coefficients are different. For example, Fig. 2 represents the static equilibrium in a PET/PE bilayer.

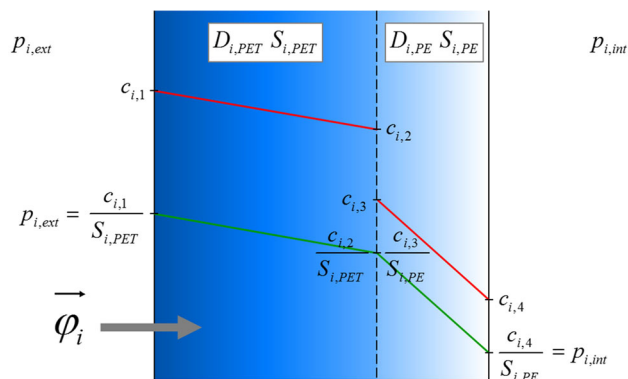


Figure 2 Gas sorption and diffusion across a PET/PE bilayer.

It is possible to obtain a continuous potential by combining both Henry's and Fick's laws. The potential $c_i/S_{i,j}$ can be studied preferably.

$$p_i = \frac{c_i}{S_{i,j}} \quad (3)$$

This potential is defined as the ratio between the gas concentration c_i at a point of the polymer and the solubility coefficient $S_{i,j}$ of this gas into the polymer j . It is continuous throughout the sample and dimensionally homogeneous with a pressure. Fick's law can be written as below:

$$\vec{\varphi}_i = -D_{i,j} S_{i,j} \vec{\nabla} \frac{c_i}{S_{i,j}} \quad (4)$$

Gas dissolution and diffusion into the defects

Defects in coating layer can be considered as pinholes which are filled either with dry air, pure water vapour or glue. When they are filled with glue, the gas transfer phenomena are exactly the same as those presented above. When they are filled with gas (dry air or pure water vapour), the sorption and diffusion phenomena are quite different.

First, the relationship between the gas concentration and the gas partial pressure is no more given by Henry's law but by the perfect gas law. The solubility coefficient has to be replaced by the inverse of the product of the specific gas constant r_i and the temperature T .

$$p_i = c_i r_i T = \frac{c_i}{\frac{1}{r_i T}} \quad (5)$$

Second, in small size defects, collisions between gas

molecules and inner walls of defects can be more frequent than collision between gas molecules. This happens when the defects diameter (\emptyset) is smaller than the mean free path of gas molecules. In such conditions the diffusion takes place according to the Knudsen process [16]. This phenomenon strongly reduces the diffusion phenomena and also explains the low thermal properties in VIPs. The diffusion coefficient in gas is replaced by the Knudsen coefficient which can be written as a function of the temperature (T), the Boltzmann constant (k_B), the molecular mass (m_i) and the defect diameter (\emptyset).

$$D_K = \frac{\emptyset}{3} \sqrt{\frac{8k_B T}{\pi m_i}} \tag{6}$$

Apparent gas permeance of a membrane

Experimental data rarely use diffusion and solubility coefficients but represent gas permeation through a macroscopic quantity which is the apparent permeance $\Pi_{i,app}$.

$$\Pi_{i,app} = \frac{\Phi_i}{A \Delta p_i} \tag{7}$$

The apparent permeance can be calculated from the apparent diffusion and solubility coefficients. The product of the diffusion and the solubility coefficient is defined as permeability.

$$\Pi_{i,app} = \frac{D_{i,app} S_{i,app}}{l} \tag{8}$$

Thermo-activation of the permeance is neglected, and simulations are made at constant temperature.

Modelling methodology and modelling tools

The study concerns a gas diffusion problem, through a 3D material and at the nanoscale. The polymer substrate layer is meshed. The aluminium is considered as perfectly impermeable to gases. All defects on the coating layer are filled either with dry air, pure water vapour or glue. So, the mesh of the films can be simplified. The aluminium does not need to be meshed, and the defects are represented by filled cylinders.

An example of a meshed barrier envelope close to a defect is represented in Figs. 3 and 4. Its geometric

parameters can be varied: the defect diameter (\emptyset), the section side length (L) and the polymer thickness (e_{poly}). We can also vary the number of defects and their position. Tetrahedral meshing is used. Only one part of the film is meshed; by symmetry and fixing boundary conditions the entire film is represented.

Analogy between heat conduction transfer and gas permeation through polymer membranes

Thermal conduction is a diffusion process very similar to the permeation problem. It is in fact possible to solve permeation problems with the thermal transfer simulation tools. The analogy between heat conduction and gas permeation equations is described in Table 1.

Temperature is replaced by the potential $c_i/S_{i,j}$, while thermal conductivity is replaced by the gas permeability, and the product of the heat capacity and the density has to be substituted by the solubility

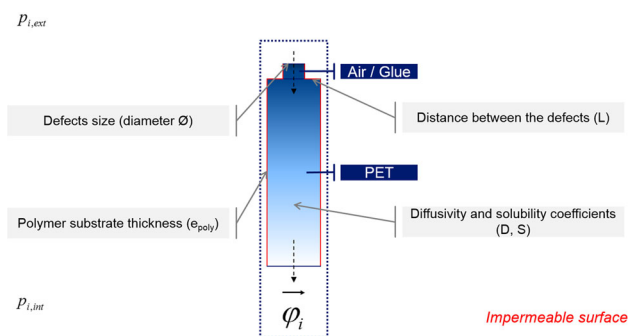


Figure 3 Schematic of the meshed pattern of PETM1F (section view), with identical and homogeneously distributed defects.

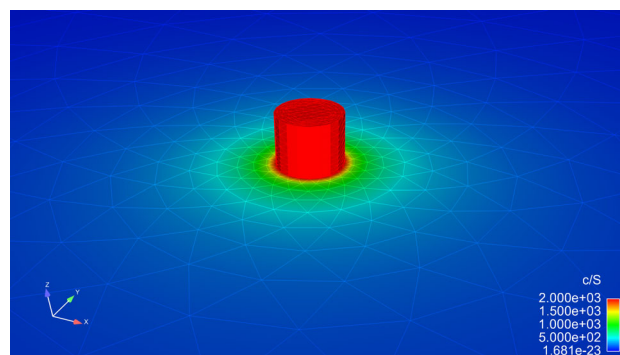


Figure 4 Mesh of the pattern of PET layer metallized on one face, with identical and homogeneously distributed defects.

Table 1 Analogy between heat conduction transfer and gas permeation through polymer membranes

Heat conduction	Mass diffusion
Temperature T	Concentration/solubility $\frac{c_{ij}}{S_{ij}}$
$\vec{\varphi} = -\lambda \vec{\nabla}(T)$	$\vec{\varphi}_i = -D_{i,j} S_{i,j} \vec{\nabla} \left(\frac{c_i}{S_{i,j}} \right)$
$\frac{\partial T}{\partial t} = \frac{\lambda}{\rho c_p} \nabla^2 T$	$\frac{\partial}{\partial t} \left(\frac{c_i}{S_{i,j}} \right) = D_{i,j} \nabla^2 \frac{c_i}{S_{i,j}}$
$\lambda \longleftrightarrow D_{i,j} S_{i,j}$ and $\rho c_p \longleftrightarrow S_{i,j}$	

coefficient. We have decided to use SYRTHES® [17] which is a finite element software developed by EDF R&D, initially created for solving 3D thermal conduction problems.

Scaling

The typical size of the studied defects is 10 nm. The meshing software does not allow the treatment of so small elements. The space variables have to be expanded, and the model physical parameters have to be adapted accordingly. For a uniform expansion by a scale factor k , the permeability (product of the diffusion and solubility coefficients) has to be multiplied by k and the solubility coefficient has to be divided by k .

Simulation results: homogeneous configurations with identical and equidistant defects

For the first simulations we assume that all the film defects can be represented with identical circular defects which are homogeneously distributed on the coating layer. The geometric parameters which can be varied are: the defect diameter (\emptyset), the distance between them (L) and the polymer thickness (e_{poly}). Surface fraction of defects (FSD) which is often an experimental characteristic can be calculated from the defect diameter and the distance between them (Eq. 9). In this study we will only use \emptyset and L parameters.

$$\text{FSD} = \frac{\emptyset}{L^2} \quad (9)$$

The physical parameters which can be varied are: the diffusion (D) and solubility (S) coefficients of the

polymer substrate layer and those of the material into defects (dry air, pure water vapour or glue).

Simulation for monolayer films

Simulations carried out here concern monolayer of polyethylene terephthalate metallized on one face. It is usually called PETM1F.

Impact of the polymer permeance

Aluminium has much better gas barrier properties than polymers. So it could be supposed that the permeance of a PETM1F film is only driven by the metallization quality. In order to evaluate this hypothesis, simulations are carried out with the same defect configuration but with different polymer permeance. We vary only the polymer diffusion coefficient. The distance between defects is fixed at 200 μm . First, we make simulations by fixing the defects diameter at 2.257 μm .

Figure 5 shows that in the value range of diffusion coefficient of PET ($10^{-13} \text{m}^2 \text{s}^{-1}$ [18–22]), the permeance is proportional to the coefficient. Beyond a certain threshold of diffusion coefficient, the permeance tends to approach a limiting value because it is no more managed by the polymer diffusion coefficient but the defects' surface.

Second, we make the same simulations by fixing the defects diameter at 50 nm. Figure 6 shows that when the defects size decreases, the threshold is lowered and the limit too. However, even modelling a PETM1F film with very few defects and as small as possible, while ensuring that their diameter is higher

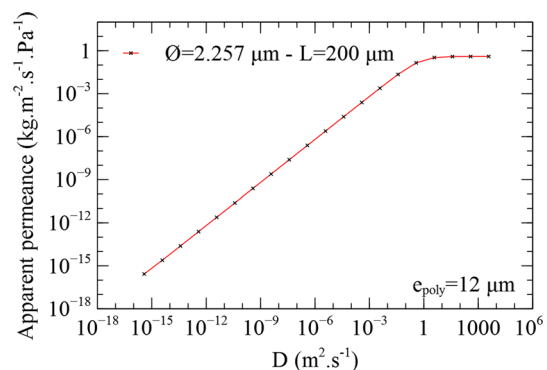


Figure 5 Theoretical apparent permeance as a function of polymer diffusion coefficient on PETM1F ($e_{\text{poly}} = 12 \mu\text{m} - \emptyset = 2.257 \mu\text{m} - L = 200 \mu\text{m}$).

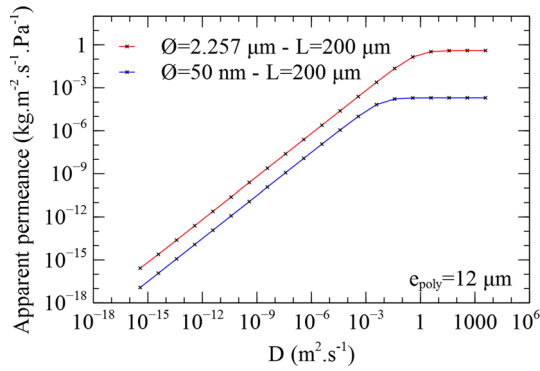


Figure 6 Theoretical apparent permeance as a function of polymer diffusion coefficient on PETM1F ($e_{poly} = 12 \mu\text{m}$ – $\emptyset = 2.257 \mu\text{m}$ and $\emptyset = 50 \text{ nm}$ – $L = 200 \mu\text{m}$).

than the one of water vapour molecule, the threshold stays several orders of magnitude higher than the diffusion coefficient of PET. The results are the same when we vary the solubility coefficient. For all the next simulations, the diffusion and solubility coefficients will be, respectively, fixed to $3.80 \times 10^{-13} \text{ m}^2 \text{ s}^{-1}$ and $2.50 \times 10^{-3} \text{ kg m}^{-3} \text{ Pa}^{-1}$ [18–20].

Hanika [9] suggested that the permeance of a polymer decreases with the thickness of the film. This result was obtained by modelling, and it was decided to perform a numerical simulation to confirm it. We varied the polymer thickness for a given number and size of flaws (cf. Fig. 7). Our simulation shows that the apparent permeance is not altered much by the polymer thickness. Only for the largest pinhole tested was the change substantial.

For all other simulations presented in this paper, the polymer thickness will be fixed to $12 \mu\text{m}$, because it corresponds to our experimental thickness.

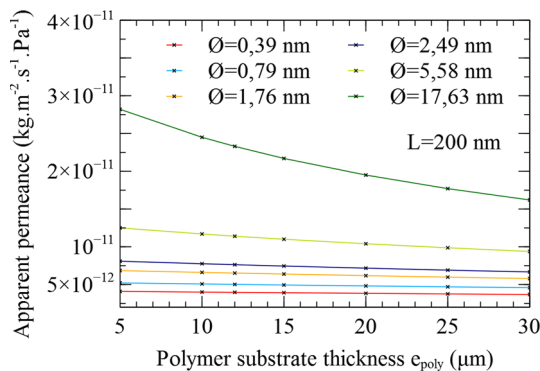


Figure 7 Theoretical apparent permeance as a function of polymer thickness for 6 defect diameters on PETM1F.

Impact of the coating layer

The following section relates the effect, on the permeation, of the nature of the material within the pinhole.

No glue in defects Several series of simulation have been carried out on PETM1F films with various density of defects, for different defect diameters and distances between defects. First, there is no glue into defects. The ranges of values chosen include the experimental data values from the bibliography [7, 9]. In Fig. 8, each continuous colour curve is an isovalue of distance between defects.

The results show that a decrease by 2 of the defect diameter and the distance between them causes a higher increase in the permeance than an increase by 2 of the defect diameter for a constant distance between them. In both cases total surface of defects is the same, but defects are not similarly distributed. In addition, when the defects become very small and close, the permeance of the PETM1F film tends to that of an uncoated PET film (represented by the red line at $7.92 \times 10^{-11} \text{ kg m}^{-2} \text{ s}^{-1} \text{ Pa}^{-1}$). In other words, in a constant surface of defects, the smaller and the more numerous the defects are, the higher the permeance is. Below a certain defect diameter (around 1 nm), the mass flow is slowed so much by the Knudsen effect in the defects that the permeance does not increase anymore, but decrease.

Glue in defects Adhesive polyurethane is used to make multilayer film. The coefficient of water vapour

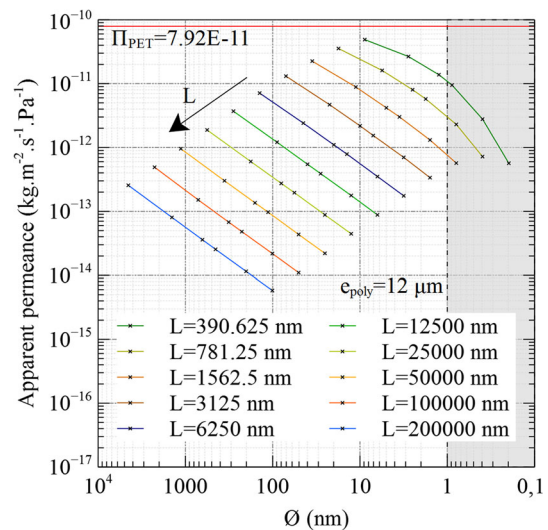


Figure 8 Calculated apparent permeance on PETM1F as a function of the defects size for 10 distances between defects.

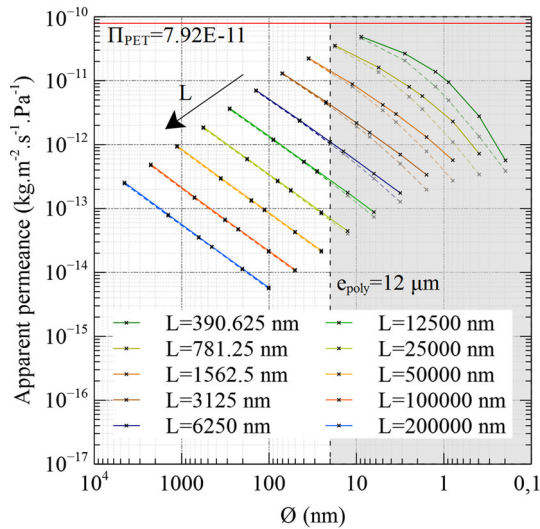


Figure 9 Calculated apparent permeance on PETM1F as a function of the defects size for 10 distances between defects, no glue in defects (continuous curves) and glue in defects (dotted curves).

in polyurethane adhesive is much lower than the self-diffusion of water vapour. If PETM1F films are modelled with adhesive in defects, the first impression is that the permeance would be lower. The simulations realized produce the results expected. Figure 9 shows that for defect diameters greater than 20 nm, the permeance values in case of adhesive in defects are very close to those without adhesive. However, for defect diameters well below 20 nm, the permeance values seem to tend towards a limit below the permeance of an uncoated PET film.

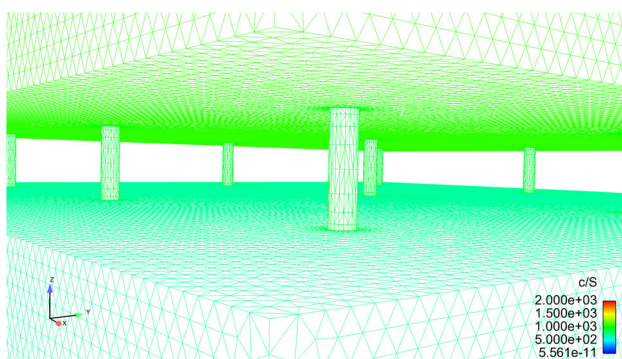


Figure 10 View of a mesh of a multilayer film, at the interface between two layers.

Simulations for multilayer films

The aim of this part is to check the validity of the ideal laminate theory (ILT). This theory has been used by several authors [23, 24] to calculate the apparent permeance Π_{app} of a multilayer film from the individual apparent permeance $\Pi_{j,app}$ of its monolayer components (Eq. 10). It is classically based on the fact that the mass transfer resistances in series can be added.

$$\frac{1}{\Pi_{app}} = \sum \frac{1}{\Pi_{j,app}} \quad (10)$$

Simulations are carried out by stacking several PETM1F which can be identical or not. Consequently, the defects can be aligned from one layer to another, or not. Figure 10 shows an example of a multilayer film mesh. At the interface between two monolayers, the defects into the aluminium coating layer have to be modelled in order to connect the two polymer substrate layers.

The simulation results for 2 PETM1F or 3 PETM1F films show that the calculated permeances respect the ILT, whatever the flow direction and the defects of the coating layers.

Interaction between defects

The independence of defects could be assumed when their size is much smaller than the distance between them. In order to confirm this intuition, the change of calculated permeance when several defects converge has been studied. As it can be imagined through the calculations carried out in paragraph 3, the flux

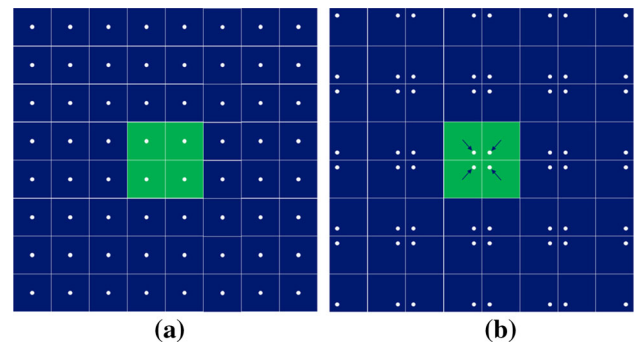


Figure 11 Schematic representation of the pattern meshed of PETM1F, with identical defects (a) and when several defects converge (b).

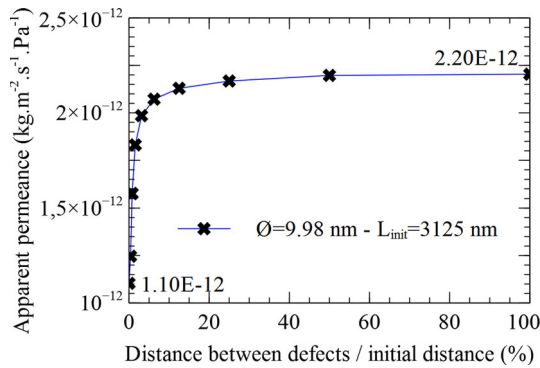


Figure 12 Theoretical apparent permeance on PETM1F as a function of the defects position.

through small defects that draw nearer and nearer should diminish to tend to that which passes through an isolated big defect that would have the accumulated size of the small defects. This part of the study is based on a new mesh for which defects can be narrowed or taken away, while the defects size and surface fraction are maintained faithfully identical (cf. Fig. 11).

Results are given in Fig. 12 which represents the apparent permeance decrease when the defects are drawing near. The simulations confirm that when the defects are very close without touching each other, the permeance is close to that obtained with an isolated big defect which has the same total area ($1.10 \times 10^{-12} \text{ kg m}^{-2} \text{ s}^{-1} \text{ Pa}^{-1}$). When the distance between the defects is divided by four, the permeance falls under 1.7%.

SEM observations in the perspective of the monolayer model validation

Scanning electron microscope (SEM) was used to take pictures of the coating layer surface of the films.

SEM observations

The films studied are PETM1F 12 μm Mylar with several coating layer thickness. The SEM used to observe the defects was a Zeiss Ultra 55 SEM and a Zeiss GeminiSEM 500 (CMTC, 38, France). The purpose is to determine which PETM1F film we can use to validate the models.

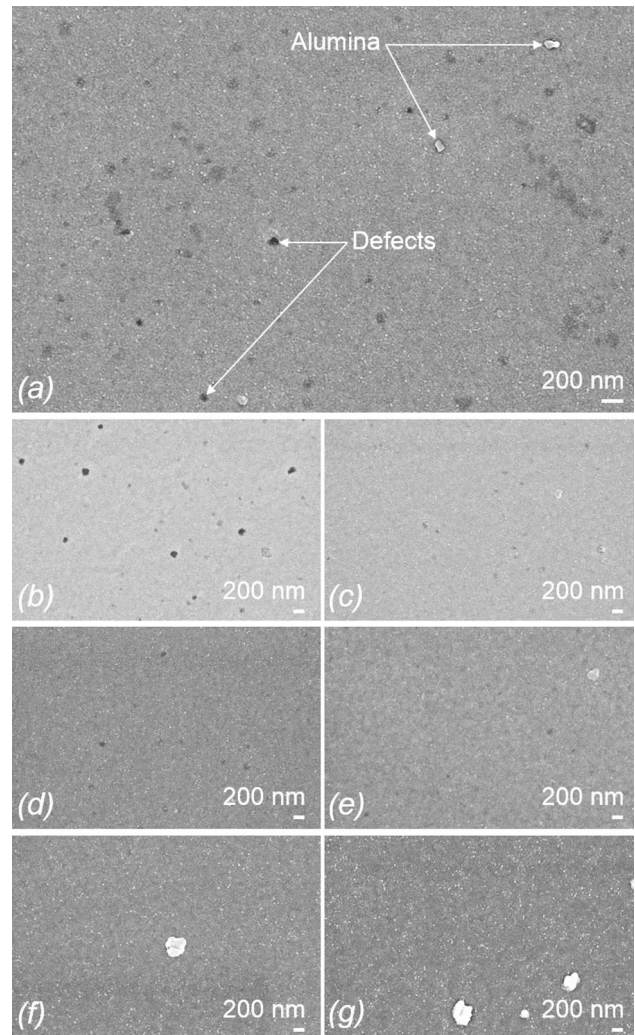


Figure 13 SEM secondary electron images of PETM1F, with Al thickness: 40 (a), 50 (b), 60 (c), 70 (d), 80 (e), 90 (f) and 100 nm (g), at magnification $\times 20\text{K}$.

Impact of the coating layer thickness

Seven different levels of coating layer thickness have been chosen: 40, 50, 60, 70, 80, 90 and 100 nm. For each thickness, a decade of images were made at four magnifications: 2K \times , 5K \times , 10K \times and 20K \times . These observations were obtained with the Zeiss Ultra 55 SEM. In order to prevent the charging of the sample, sputter coating of gold/palladium (Au/Pd) for SEM is realized. Only the SEM images of PETM1F at magnification 20K \times are presented in Fig. 13.

For the PETM1F 40 and 50 nm (Fig. 13a, b), the pinholes on the aluminium coating layer are clearly visible and numerous (black spots). We can distinguish several sizes of defects. The bigger ones ($> 50 \text{ nm}$) seem to be further away from each other

than the smaller ones (<50 nm). Unlike some of the authors [7, 25–27] who have observed macrodefects ($> 1 \mu\text{m}$), all the defects observed are of submicron size. This can be explained by the enhancement of films and the improvements in the production process.

For the PETM1F 60 and 70 nm (Fig. 13c, d), it is very difficult to observe the smaller defects, and the bigger ones are fewer. From 80 nm of aluminium thickness (Fig. 13e–g), it is no longer possible to observe any defects at this magnification. We can see white spots which can be considered as alumina particles.

In view of the SEM observations, the PETM1F 40 nm is chosen to be the support of the model validation. The image processing is explained in “Image processing” section.

Because the PETM1F film with 80, 90 and 100 nm of aluminium coating is not perfectly impermeable to the water vapour, we can suppose that there are still small defects. These defects are not visible either because the magnification is not high enough, or because the sputter coating prevents to observe them. The purpose of the second series of simulations is to try to observe defects on films with high metallization thickness and with higher magnification and resolution.

Impact of the sputter coating thickness

During the sputter coating process, we apply an ultra-thin coating of gold/palladium which permits to increase the amount of secondary electrons that can be detected in the SEM and the signal-to-noise ratio. But this Au/Pd coating could fill the very small defects of the Al coating and therefore prevent their observation, more specifically with larger metallization thicknesses.

The SEM images of Fig. 14, obtained with the Zeiss GeminiSEM 500, show the PETM1F 80-nm surface with 1 nm (a) and 0.7 nm (b) of Au/Pd and without Au/Pd (c), at magnification $100K\times$. Other observations with an ESEM were made, but the resolution is not of sufficiently high quality.

We can clearly see the aluminium grains. The lower the Au/Pd thickness is, the better the recognition is. The average size of grains is about 30–50 nm. In Fig. 14a, b, the sputter coating corresponds to the very small grains which are much smaller than the aluminium grains. In Fig. 14c, it is

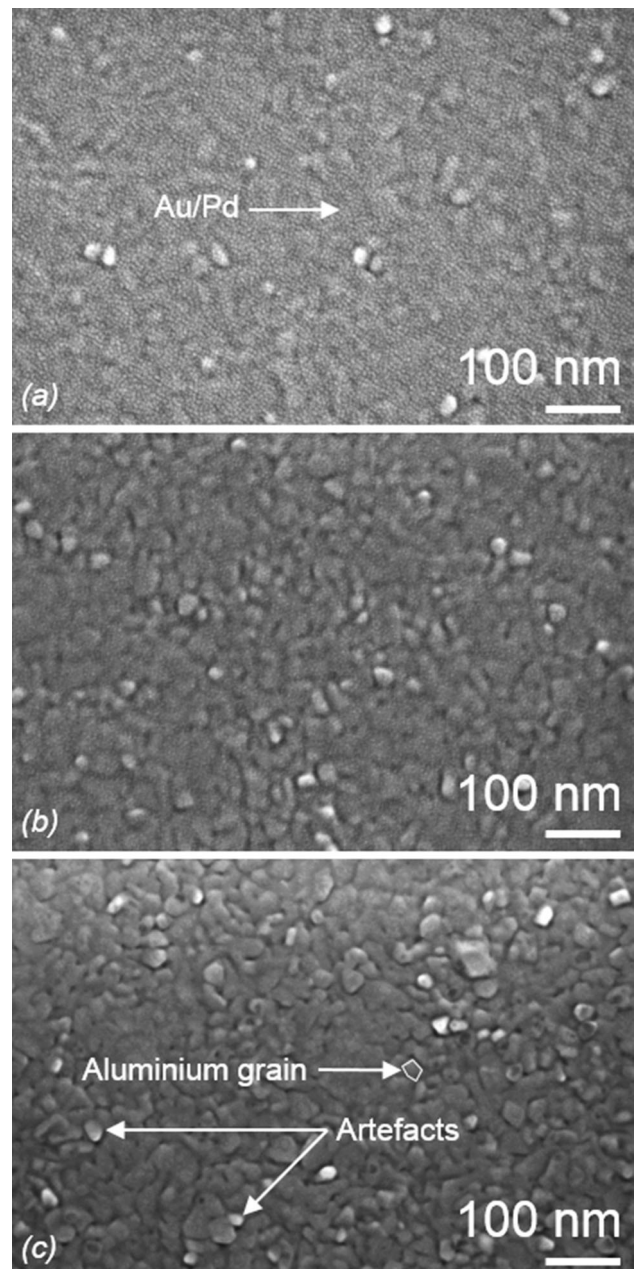


Figure 14 SEM secondary electron images of PETM1F 80 nm, with Au/Pd thickness: 1 nm (a), 0.7 nm (b); without Au/Pd (c), at magnification $\times 100K$.

possible to distinguish some very small black pin-holes between the aluminium grains, but it is difficult to state with certainty that these are really defects. Furthermore, the white spots could be an artefact due to the surface geometry of the aluminium.

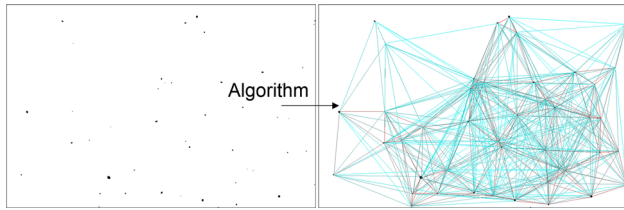


Figure 15 Binarized image of PETM1F 40 nm (magnification $\times 10K$, $11.77 \times 7.70 \mu\text{m}^2$) and application of the algorithm which calculates the distances between the defects.

Image processing

An image processing tool has been used to analyse the defects and the distance between them in order to construct a statistic distribution of defects. The image processing of SEM images of PETM1F 40-nm films with magnification $5K\times$ and $10K\times$ has been carried with the ImageJ[®] software.

It is possible to split the image processing into different steps. The initial step consists of preparing the images: cut them, calculate the scale, harmonize the brightness and the contrast, reduce the image noise, and then realize the binarization. With these binarized images we apply algorithms to determine: the surface of each defect, its position and the distance which separates it from the others. Figure 15 shows the calculated distances between one defect and its neighbours from one binarized image.

From this image processing, the surface distribution and the distance distribution have been estimated for 9 SEM images at magnification $5K\times$ and $10K\times$. Only the results with magnification $10K\times$ are presented (cf. Figs. 16 and 17). The mean defect size

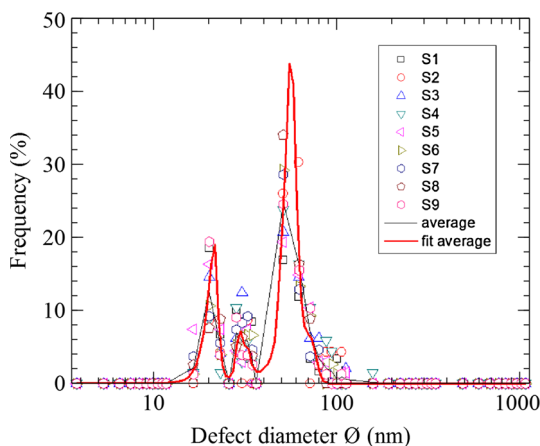


Figure 16 Defects surface distribution, on PETM1F 40 nm with magnification $\times 10K$.

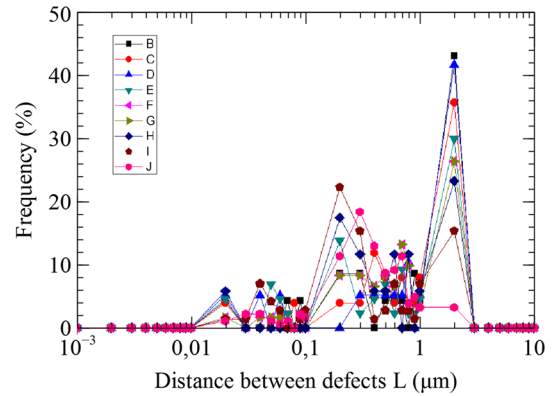


Figure 17 Distance between defects distribution, on PETM1F 40 nm with magnification $\times 10K$.

is around 47 nm, and the mean distance which separates them is around 1.40 µm.

Nevertheless, 3 populations of defect sizes about 20, 30 and 56 nm of diameter can be determined. The proportions of these populations are, respectively, 4.3, 4.1 and 91.6%. Regarding the distances between the defects, we can only select 2 mean values: 0.41 µm for the smaller populations 1 and 2, and 1.75 µm for the bigger population 3. The total surface fraction of defects is equal to $0.12 \pm 0.03\%$. The image resolution induces a large uncertainty on the size of the pin-holes. The results are recapped in Table 2 in the next paragraph.

The algorithms also permit to determine the size of each defect and its exact position on the coating layer.

Model validation

The experimental permeances are compared to the calculated permeances from the model with identical and equidistant defects. The defect characteristics are those that have been determined in the previous paragraph from the SEM images with magnification $10K\times$. The mean defect diameter is 47 nm, and the mean distance which separates them is 1.40 µm. The comparison between experimental and calculated values of permeances is presented in Table 3.

It can be seen that the calculated values are about 60 times higher than the experimental values. It can be suspected that the coating defects cannot be represented by a homogeneous distribution of pinholes, and that a more realistic distribution should be adopted in order to take into account more accurately the interactions between defects.

Table 2 Analysis results of the image processing on PETM1F 40-nm film, with magnification 10K \times

Analysis Mag. 10K \times	Diameter \emptyset (nm)	Distance L (μm)	Proportion (%)
Pop. 1	20 ± 19.5	0.41 ± 19.5	4.3
Pop. 2	30 ± 19.5	0.41 ± 19.5	4.1
Pop. 3	56 ± 19.5	1.75 ± 19.5	91.6

Table 3 Calculated permeance of PETM1F 40 nm, from the model with identical and equidistant defects

Model validation on PETM1F 40 nm Mag.10K \times	Experimental permeance [7, 9] ($\text{kg m}^{-2} \text{s}^{-1} \text{Pa}^{-1}$)	Calculated permeance ($\text{kg m}^{-2} \text{s}^{-1} \text{Pa}^{-1}$)
Model 1 Identical and equidistant defects ($\emptyset = 47 \text{ nm}$, $L = 1.40 \mu\text{m}$)	$9.00 \times 10^{-13} < \Pi < 1.36 \times 10^{-12}$	6.11×10^{-11}

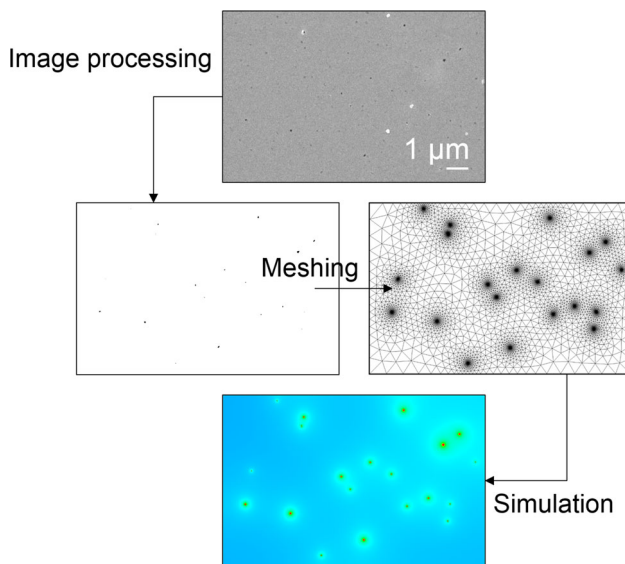


Figure 18 Modelling of PETM1F 40 nm with real population of defects: image processing, meshing and simulation.

Model with several classes of defects In a second attempt, it is proposed to calculate the permeance by meshing 3 classes of defects defined by their size and the distance which separates them as a function of the statistic distributions given in Figs. 16 and 17.

Model with real population of defects In the third attempt, the coating defects have been meshed as they appeared on the SEM images (cf. Figs. 18 and 19).

The comparison between the new calculated permeances and the experimental ones is presented in Table 4.

The calculated permeance with the more realistic configurations is closer to the experimental result, but remained significantly higher. This means that

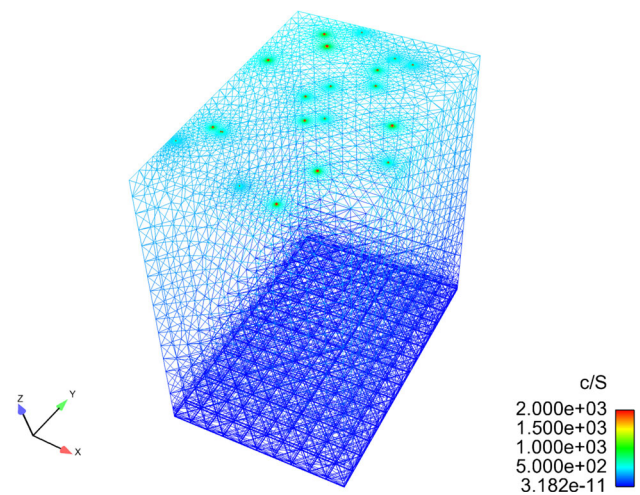


Figure 19 Mesh of PETM1F, with not identical and not homogeneously distributed defects.

interaction between defects has a significant impact, but that modelling hypothesis adopted here fails to accurately estimate the actual PETM1F permeance.

Discussion about results

SEM observations The SEM observations enabled us to see the real defects of a PETM1F-coated layer. Obviously, the increase in the aluminium thickness leads to smaller and less numerous defects. The coating of gold/palladium can be observed but does not disturb the observation of the defects. It is possible to distinguish the aluminium grains, but the observation is more complicated and has to be done with high magnification and without sputter coating process.

Table 4 Calculated permeance of PETM1F 40 nm, from the model with several classes of defects and the model with real population of defects

Model validation on PETM1F 40 nm Mag. 10K×	Experimental permeance [7, 9] (kg m ⁻² s ⁻¹ Pa ⁻¹)	Calculated permeance (kg m ⁻² s ⁻¹ Pa ⁻¹)
Model with 3 populations of defects ($\phi_1 = 20$ nm, $L_1 = 0.41$ μ m $\phi_2 = 30$ nm, $L_2 = 0.41$ μ m $\phi_3 = 56$ nm, $L_3 = 1.75$ μ m)	$9.00 \times 10^{-13} < \Pi < 1.36 \times 10^{-12}$	55.9×10^{-12}
Model with real population of defects		16.1×10^{-12}

In practice, beyond 70 nm of aluminium, no defect can be observed by SEM observation. But the permeance of these films being not equal to zero, the defects cannot totally explain the mass flows which pass through the films. So, a diffusion phenomenon between the grain boundaries could be possible.

For small coating thicknesses (below 50 nm), image processing allows the determination of defect characteristics (diameter and mean distance between them). Nevertheless, the calculation of the mean size of defect is less precise due to the resolution limitation. The margin of error can be up around $\pm 97\%$.

Simulations The simulations have demonstrated that the permeance of a PETM1F depends both on the defects in the coating layer and on the gas transfer properties of the polymer substrate. As mentioned in the literature [8, 9], simulations confirm that the permeance is proportional to the diffusion and solubility coefficients and is inversely proportional to the polymer thickness.

The simulations carried out with homogeneous defect distributions on PETM1F confirmed that the permeance depends more on the number of defects than on the cumulated surface of defects. This can be explained by the fact that with narrow pinholes, the mean distance that gas molecules have to go through the polymer is close to the polymer thickness. At the limit, the permeance tends to that of the uncoated film. However, if defects are smaller than 1 nm, the permeance is limited by the Knudsen effect in the defects. When defects are filled with glue, for defect diameters well below 20 nm, the permeance values seem to tend towards a limit below the permeance of an uncoated PET film.

Nevertheless, due to the high viscosity of glue, it is unlikely that it can enter into defects of a few tens of nanometre size. So, the permeance values from simulations without adhesive in defects are potentially closer to real values.

Validation attempts show that calculated permeances are significantly over estimated. Even for the more favourable configurations the calculated permeances are more than 10 times too high. Several hypothesis could explain that difference. They are listed and discussed below.

- The first hypothesis is that the measured permeances are systematically underestimated. Gas leaks in the upstream chamber of the permeameter would cause an increase in the total pressure, and a not perfect degassing of the sample, before the measurement, would let dry air molecules in it. The sample would be not only in water vapour but also in dry air. Therefore, it has been shown that the permeance of each gas decreases with increasing the other gas due to a coupling between gases. So if the measurements are not realized in perfect conditions and in pure gas, the measurement is underestimated. On the other hand, the measurements were taken very carefully. Leaks would be detected by a pressure increasing, and the degassing is realized at least long enough. So, it is very unlikely that this hypothesis would be the explication.
- Another hypothesis is that the polymer transfer characteristics change because of coating. Indeed, the diffusion and solubility coefficients put in the models are those measured on the polymer substrate uncoated, but not directly on the metallized film. The values of these coefficients could be different. However, some measurements of the crystallinity and the solubility coefficient realized on PETM1F films do not show any difference. We can conclude that it is unlikely that the diffusion coefficient would be different, while the crystallinity remains the same.
- About the diffusion coefficient, we have considered in the models, the polymer as isotropic. But

some authors [28–30] have observed an anisotropy in Bi-oriented PET or PET. We have made simulations by varying the diffusion coefficients in both directions. The results show that the diffusion coefficient in the plane has to be around 100 times lower than that of transverse, to decrease the permeance by a factor 10. These results lead us to disprove this hypothesis.

- It has also been suggested the hypothesis that all the black spots observed with SEM would not be real defects through the coated layer. The binarization and the image processing are manually realized, and this induces uncertainties on the number of defects and their size. Furthermore, it was difficult to observe with accuracy the defects due to the compromise between resolution and observed area. Some black spots are darker than others, and it is not possible to identify with certainty that the brightest ones are real defect through the coated layer. But we can remark the good correlation between the observation and the permeances measured. The lower we observe defects on PETM1F with different coated layer thickness, the lower the permeance is.
- The last hypothesis, but not least probable, suggests a potential interaction between the water vapour and the aluminium. The water vapour flow passing through the defects or the grain boundaries of aluminium would be slowed down by a physical or chemical interaction. We can suppose that this interaction could be altered by changing the metal.

Several of these hypothesis combined would explain the difference between the permeances calculated by the developed models and measured.

Coupling between water vapour and dry air permeance
The aim of this part is to study the hypothesis of coupling between water vapour and dry air permeance. Water vapour permeance measurements were realized by varying dry air pressure, and then, dry air permeance measurements were realized by varying water vapour partial pressure. Coated and uncoated PET films have been studied.

First, water vapour permeance measurements were realized on PET Mylar M841 12 μm films uncoated and metallized on one face with 100 nm of aluminium, at 50 °C and 40% RH (water pressure $P_v = 4933$ Pa) and at different dry air upstream pressures. A Deltaperm from Technolox [31] was used. The

measured permeances values are presented in Figs. 20 and 21.

We can observe that for both films, the water vapour permeance decreases and is inversely proportional to the dry air pressure increases.

For the uncoated PET film, the water vapour permeance decrease is important and varies from 3.05×10^{-12} to 8.50×10^{-13} $\text{kg m}^{-2} \text{s}^{-1} \text{Pa}^{-1}$ when the dry air pressure increases from 14665 to 97325 Pa. The measured values are from 10 and 100 times lower than the permeances usually measured for pure water vapour. For the coated film, the decrease is less obvious and the measured values are in the same order of magnitude as that of measured for pure water vapour. The water vapour permeance decreases from 5.30×10^{-13} to 2.67×10^{-13} $\text{kg m}^{-2} \text{s}^{-1} \text{Pa}^{-1}$ when the dry air pressure increases from 13865 to 91192 Pa.

Measurements have been realized in order to study the impact of the water vapour pressure on the dry

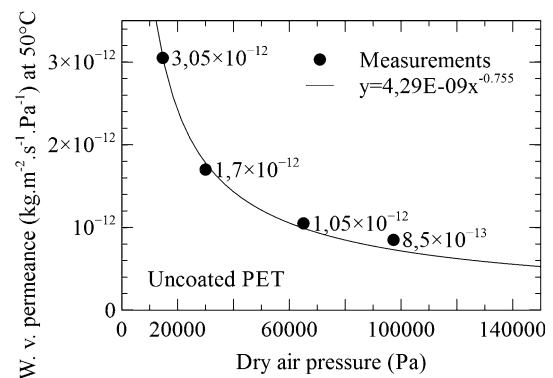


Figure 20 Water vapour permeance (at 50 °C) regarding the dry air pressure, for the uncoated PET 12 μm film.

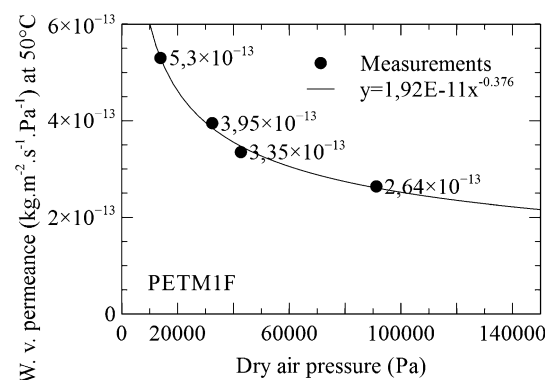


Figure 21 Water vapour permeance (at 50 °C) regarding the dry air pressure for the PET 12 μm M1F 100-nm film.

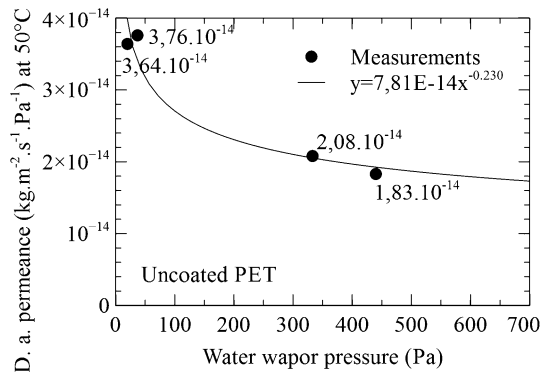


Figure 22 Dry air permeance (corrected at 50 °C) regarding to the water vapour partial pressure, for the uncoated PET 12 μm film.

air permeance. As air permeances are much smaller than water vapour permeances, the tests were only carried out with uncoated PET film, with several upstream water vapour partial pressures and at different temperatures varying from 30 to 60 °C. Figure 22 shows the dry air permeance values rectified at 50 °C.

We note that the dry air permeance also depends on the water vapour partial pressure. The dry air permeance decreases from 3.76×10^{-14} to $1.83 \times 10^{-14} \text{ kg m}^{-2} \text{ s}^{-1} \text{ Pa}^{-1}$ when the water vapour partial pressure increases from 20 to 440 Pa. It is also possible to fit the curve with a power law. Obviously, water vapour and dry air transfer characteristics cannot be considered as independent.

Conclusion and outlooks

All simulations and experimental work presented in this paper aim at improving our understanding of the mass transfer phenomena through the VIPs barriers. The numerical model could not be quantitatively validated. But the qualitative results highlight the impact of the defects distributions and characteristics on the films' permeance. We were able to better understand the different mechanisms and diffusion regimes involved.

The SEM observations enabled us first of all to detect defects on the coated layer and aluminium grains. The increase in the aluminium thickness leads to smaller and less numerous defects. Beyond 70 nm it was not possible to detect defects with the SEM on the films studied. This could be in favour of the

hypothesis of a diffusion phenomenon through the grain boundaries. In any cases, the diffusion does not take place without interaction with the aluminium coating.

The results lead us to become quite involved in the interaction between the gases and the coated layer on the one hand and the coupling between these gases on the other hand.

Acknowledgements

The authors gratefully acknowledge the collaborators of the Project EMMA-PIV (No. ANR 12-VBDU-0004-01) that includes this research and also the National Research Agency (ANR) for his financial support. Thanks also to the "Consortium des Moyens Technologiques Communs" (CMTC, 38, France) for his contribution to the SEM observations. This work is performed within the framework of the Centre of Excellence of Multifunctional Architected Materials "CEMAM" No. AN-10-LABX-44-01.

References

- [1] Erb M, Simmler H, Brunner S, Heinemann U, Schwab H, Kumaran K, Mukhopadhyaya P, Quenard D, Sallee H, Noller K, Kucukpinar-Niarchos E, Stramm C, Cauberg MTH (2005) Vacuum insulation panels—study on VIP-components and panels for service life—prediction of VIP in building applications (subtask A). Tech. Rep. Sept 2005, HiPTI—High Performance Thermal Insulation—IEA/ECBCS Annex 39
- [2] CSTB (2005) Quelle durabilite des produits de construction?
- [3] ISO (2014) NF ISO 15686—bâtiments et biens immobiliers construits, pp 1–11
- [4] Garnier G, Marouani S, Yrieix B, Pompeo C, Chauvois M, Flandin L, Brechet Y (2011) Interest and durability of multilayers: from model films to complex films. *Polym Adv Technol* 22(6):847–856. <https://doi.org/10.1002/pat.1587>
- [5] Schwab H, Heinemann U, Beck A, Ebert H-P, Fricke J (2005) Permeation of different gases through foils used as envelopes for vacuum insulation panels. *J Therm Envel Build Sci* 28(4):293–317. <https://doi.org/10.1177/1097196305051791>
- [6] Garnier G, Quenard D, Yrieix B, Chauvois M, Flandin L, Brechet Y (2007) Optimization, design, and durability of vacuum insulation panels. In: 8th international vacuum insulation symposium (1), pp 1–8

- [7] Garnier G, Yrieix B, Brechet Y, Flandin L (2010) Influence of structural feature of aluminum coatings on mechanical and water barrier properties of metallized pet films. *J Appl Polym Sci* 115(5):3110–3119. <https://doi.org/10.1002/app.31372>
- [8] Hanika M, Langowski HC, Moosheimer U, Peukert W (2003) Inorganic layers on polymeric films—influence of defects and morphology on barrier properties. *Chem Eng Technol* 26(5):605–614. <https://doi.org/10.1002/ceat.200390093>
- [9] Hanika M (2004) Zur permeation durch aluminiumbedampfte polypropylen- und polyethylenterephthalatfolien, Ph.D. thesis
- [10] Miesbauer O, Schmidt M, Langowski HC (2008) Stofftransport Durch Schichtsysteme aus Polymeren und Dünnen Anorganischen Schichten, vol 20, pp 32–40. Wiley. <https://doi.org/10.1002/vipr.200800372>
- [11] Miesbauer O (2017) Analytische und numerische Berechnungen zur Barrierewirkung von Mehrschichtstrukturen. Tech. rep., Technische Universität München, München. <http://mediatum.ub.tum.de/?id=1340275>. Accessed 19 Mar 2018
- [12] Stannett V (1968) Simple gases. In: Crank J, Park GS (eds) *Diffusion in polymers*. Academic Press, New York, pp 41–73
- [13] Hopfenberg HB, Stannett V (1973) *The diffusion and sorption of gases and vapours in glassy polymers*. Springer, Dordrecht, pp 504–547
- [14] Flaconnèche B, Martin J, Klopffer MH (2001) Permeability, diffusion and solubility of gases in polyethylene, polyamide 11 and poly(vinylidene fluoride). *Oil Gas Sci Technol* 56(3):261–278. <https://doi.org/10.2516/ogst:2001023>
- [15] Klopffer MH, Flaconnèche B (2001) Transport properties of gases in polymers: bibliographic review. *Oil Gas Sci Technol* 56(3):223–244. <https://doi.org/10.2516/ogst:2001021>
- [16] He W, Lv W, Dickerson JH (2014) *Gas diffusion mechanisms and models*. Springer, Cham, pp 9–17. https://doi.org/10.1007/978-3-319-09737-4_2
- [17] EDF, Rupp I, Peniguel C (2015) *Syrthes*, version 4.3
- [18] Pons E, Yrieix B, Heymans L, Dubelley F, Planes E (2015) Permeation of water vapor through high performance laminates for VIPs and physical characterization of sorption and diffusion phenomena. *Energy Build* 85:604–616. <https://doi.org/10.1016/j.enbuild.2014.08.032>
- [19] Shigetomi T, Tsuzumi H, Toi K, Ito T (1999) Sorption and diffusion of water vapor in poly(ethylene terephthalate) film. *Polymer* 76(1):67–74
- [20] Launay A, Thominet F, Verdu J (1999) Water sorption in amorphous poly(ethylene terephthalate). *J Appl Polym Sci* 73(7):1131–1137. [https://doi.org/10.1002/\(SICI\)1097-4628\(19990815\)73:7<1131::AID-APP403.0.CO;2-U](https://doi.org/10.1002/(SICI)1097-4628(19990815)73:7<1131::AID-APP403.0.CO;2-U)
- [21] Rueda DR, Varkalis A (1995) Water sorption/desorption kinetics in poly(ethylene naphthalene-2,6-dicarboxylate) and poly(ethylene terephthalate). *J Polym Sci Part B Polym Phys* 33(16):2263–2268
- [22] Yasuda H, Stannett V (1962) Permeation, solution, and diffusion of water in some high polymers. *J Polym Sci* 57(165):907–923. <https://doi.org/10.1002/pol.1962.1205716571>
- [23] Langowski HC (2008) Permeation of gases and condensable substances through monolayer and multilayer structures, pp 297–347. <https://doi.org/10.1002/9783527621422.ch10>
- [24] Schrenk WJ, Alfred TJ (1969) Some physical properties of multilayered films. *Polym Eng Sci* 9(6):393–399
- [25] Singh B, Bouchet J, Rochat G, Leterrier Y, Manson JE, Fayet P (2007) Ultra-thin hybrid organic/inorganic gas barrier coatings on polymers. *Surf Coat Technol* 201(16–17):7107–7114. <https://doi.org/10.1016/j.surfcoat.2007.01.013>
- [26] Roberts AP, Henry BM, Sutton AP, Grovenor CRM, Briggs GAD, Miyamoto T, Kano M, Tsukahara Y, Yanaka M (2002) Gas permeation in silicon-oxide/polymer (SiO_x/PET) barrier films: role of the oxide lattice, nano-defects and macro-defects. *J Membr Sci* 208(1–2):75–88. [https://doi.org/10.1016/S0376-7388\(02\)00178-3](https://doi.org/10.1016/S0376-7388(02)00178-3)
- [27] Rochat G, Leterrier Y, Fayet P, Manson J-AE (2005) Influence of substrate additives on the mechanical properties of ultrathin oxide coatings on poly(ethylene terephthalate). *Surf Coat Technol* 200(7):2236–2242
- [28] Cakmak M, Spruiell JE, White JL, Ye JSL (1987) Small angle and wide angle X-ray pole figure studies on simultaneous biaxially stretched poly(ethylene terephthalate) (PET) films. *Polym Eng Sci* 27(12):893–905. <https://doi.org/10.1002/pen.760271205>
- [29] Karacan I (2005) An in depth study of crystallinity, crystallite size and orientation measurements of a selection of poly(ethylene terephthalate) fibers. *Fiber Polym* 6(3):186–199. <https://doi.org/10.1007/BF02875642>
- [30] Carr JM, MacKey M, Flandin L, Schuele D, Zhu L, Baer E (2013) Effect of biaxial orientation on dielectric and breakdown properties of poly(ethylene terephthalate)/poly(vinylidene fluoride-co-tetrafluoroethylene) multilayer films. *J Polym Sci Part B Polym Phys* 51(11):882–896. <https://doi.org/10.1002/polb.23277>
- [31] Nurenberg H, Hoshi S, Kondo T (2008) Measurement of water vapor permeation in the range of e^{-3} and e^{-5} g/m²/day for applications in flexible electronics. Tech. Rep. 1